Trikafta rescues F508del-CFTR by tightening specific phosphorylation-dependent interdomain interactions

Running title: Correction pathway of ΔF508-CFTR

Guangyu Wang[1,2]*

[1]Department of Physiology and Membrane Biology, University of California School of Medicine, Davis, California, USA

[2]Department of Drug Research and Development, Institute of Biophysical Medico-chemistry, Reno, Nevada, USA

* Correspondence E-mail: gary.wang10@gmail.com

Abstract

Trikafta is well-known for correcting the thermal and gating defects caused by the most common cystic fibrosis mutation F508del in the human cystic fibrosis transmembrane conductance regulator even at physiological temperature. However, the exact pathway is still unclear. Here, the noncovalent interactions among two transmembrane domains (TMD 1 and TMD2), the regulatory (R) domain and two nucleotide binding domains (NBD1 and NBD2), along with the thermoring structures of NBD1, were analyzed around the active gating center. The results demonstrated that Trikafta binding to TMD1 and TMD2 rearranged their interactions with the R domain, releasing the C-terminal region from NBD1 for its tight ATP-dependent dimerization with NBD2, stabilizing NBD1. Taken together, although the deletion of F508 induces the primary thermal defect of NBD1 and then the gating defect at the TMD1-TMD2 interface, Trikafta rescued them in a reverse manner allosterically. Thus, the thermoring structure can be used to uncover the pathway of a drug to correct the thermal defect of health-related protein. (160 words).

Key words: allosteric correction; digital biology; gating center; grid thermodynamic signature; least-stable interaction; noncovalent structure; melting threshold; protein stability.

Significance:

Trikafta modulators have been approved by the FDA to treat the most common cystic fibrosis–causing mutation F508del CFTR. However, the molecular action mechanisms of these modulators are still unknown. Following the identification of the gating center in CFTR, this study further revealed that the specific noncovalent interactions of the phosphorylated S813 site with cytoplasmic loops 1 and 4 and N-/C- terminal tails of TMD1 upon Trikafta-triggered tight TMD1-TMD2 interactions at the gating center play a pivotal role in rescuing the primary gating defect and then the thermal defect of F508del CFTR.

Highlights:

- Trikafta strengthened TMD1-TMD2 interactions at the gating center of ΔF508-CFTR
- Tight TMD1-TMD2 interactions allowed specific interactions of the R domain with the ICL1-ICL4 interface and the N-/C- terminal tails of TMD1
- Subsequently, the C-terminal region was released from NBD1 for tight ATP-dependent NBD1-NBD2 dimerization, stabilizing NBD1 of ΔF508-CFTR

INTRODUCTION

Cystic fibrosis (CF) is the most common fatal genetic disease in the Caucasian population and is also prevalent in other human populations. On the other hand, secretory diarrhea is the leading cause of infant mortality worldwide. A key factor in both of these devastating diseases is a protein called Cystic Fibrosis Transmembrane conductance Regulator (CFTR) with activity too low or high. It belongs to the family of ATP-binding cassette (ABC) transporters but functions as a phosphorylation-dependent and ATP-gated chloride/anion channel. It regulates salt–water balance of the lung, intestine, pancreas, and sweat once expressed on the cell plasma membrane in epithelial tissues around the human body (1-4). To date, more than 2000 mutations in CFTR have been found to cause CF (http://www.genet.sickkids.on.ca/cftr; CFTR2 database: https://cftr2.org). The most common mutation (70 % of CF cases) is ΔF508, which has both gating and thermal defects, leading to bacterial infection and respiratory failure (4-13).

A cryo-electron microscopy (cryo-EM) structure of dephosphorylated human CFTR (PDB, 5UAK) reveals that it starts with a lasso motif (1-37) and is composed of five domains in the following order: transmembrane domain 1 (TMD1) (38-383), nucleotide binding domain 1 (NBD1) (384-645), the regulatory (R) domain (646-843), transmembrane domain 2 (TMD2) (844-1172), and nucleotide binding domain 2 (NBD2) (1173-1436). Both TMD1 and TMD2 line an anion conduction pathway with each consisting of six transmembrane (TM) helices, which extend to the intracellular loops (ICLs). The arrangement of TM1, 2, 3 and 6 forming a bundle with TM10 and 11 while the remaining TM helices shaping another bundle allows for domain swapping. This enables NBD1 to primarily connect with TMD2 via ICL4 and NBD2 to mainly relate to TMD1 via ICL2 (14). When the R domain is phosphorylated by protein kinase A (PKA) for Mg/ATP-mediated NBD1-NBD2 dimerization (15), the hydrolysis-deficient E1371Q mutant is open with distinct NBD1-ICL4 and NBD2-ICL2 interactions (15, 16).

In contrast, for the most common cystic fibrosis-causing ΔF508 mutant that primarily destabilizes NBD1 and the nearby interdomain interactions (17-21), even if a type I corrector like lumacaftor (VX-809) is bound to TMD1 in the phosphorylated and ATP-bound conformation to secure the channel expression on the cell surface, NBD1 folding remains flexible until the folding corrector tezacaftor (VX-661), the folding and gating modulator elexacaftor (VX-445) and the channel activity potentiator ivacaftor (VX-770) in Trikafta (branded as Kaftrio in Europe) are bound to TMD1 and TMD2, completely restoring Δ508 to an NBD-dimerized conformation with

ATP fully occluded both the consensus and degenerate sites (22). In this case, although the gating and thermal defects of ΔF508-CFTR are synergistically rescued by Trikafta at 37 °C (23-27), much less is known about the exact pathway.

On the other hand, while the thermostability of isolated hNBD1 can be measured using differential scanning calorimetry (DSC) or differential scanning fluorimetry (DSF) (9,11, 28-29), directly measuring NBD1's thermostability with either biophysical approach becomes impossible in the presence of various interdomain interactions when it is not isolated from the full-length hCFTR. Therefore, an alternative tool is necessary to assess the effects of adjacent interdomain interactions on NBD1's thermostability, allowing the rescuing pathway of the thermal defect of ΔF508 CFTR by Trikafta to be unveiled even within such a complex multi-domain protein.

Recently, a novel and highly sensitive graphical method has been developed to analyze the structural thermo-stability and functional thermo-activity of proteins including enzymes. Based on their high-resolution 3D structures, the tertiary noncovalent interactions can be constrained by a grid thermodynamic model as the thermoring structures along the single peptide. When the biggest thermoring is identified, the melting temperature threshold to unfold the least-stable noncovalent interaction along the single peptide can be calculated. Because both theoretical and experimental values matched well for isolated human NBD1 (hNBD1) upon different structural perturbations (30), this graphical analysis can be applicable to this study to evaluate the effects of the interdomain interactions on NBD1's thermostability within the full-length hCFTR. The results demonstrated that Trikafta could rescue both gating and thermal defects of ΔF508 from tight TMD1-TMD2 interactions at the gating center to the specific binding of the R domain to the ICL1-ICL4 interface, and then to the release of the C-terminal region from NBD1 for its tight Mg/ATP-mediated dimerization with NBD2 to stabilize NBD1. Thus, the thermoring structural analysis is indispensable for uncovering Trikafta's correction pathway.

RESULTS

NBD1-ICL4 interactions fail to increase the melting threshold of hNBD1

The isolated hNBD1-Δ(RE, RI) (PDB, 2PZE) is a single peptide spanning from S386 to G646 with a segment 405-436 deleted (28). In contrast, the dephosphorylated hNBD1 in full-length CFTR (PDB, 5UAK) has disordered RI (403-438) and RE (647-678) (14). Therefore, in the absence of Mg/ATP-mediated NBD1-NBD2 dimerization, it is interesting to compare their melting

temperature thresholds to evaluate the effects of NBD1-ICL4 interactions alone on the thermal stability of hNBD1.

In the dephosphorylated state, NBD1 is separated from NBD2. Without Mg/ATP bound, NBD1 had ten H-bonds, two salt bridges and seven π interactions (Figures 1a & S1). Most of these noncovalent interactions formed smaller thermorings. For example, a smaller $Grid_5$ had a 5-residue size to control the F508-R560 and Y517-Y563 π bridges via a thermoring from F508 to Y512, Y517, Y563, R560 and back to F508. In addition, both the K584-E608 salt bridge and the E383-K606 H-bond were governed by a smaller thermoring $Grid_1$ from K584, E608, K606, E583 and back to K584. In contrast, some H-bonds generated bigger thermorings. For example, when the side chain of N597 H-bonded with the backbone NH at G451, a bigger $Grid_{15}$ had a 15-residue size to control the N597-G451 and R450-D567 H-bonds via a thermoring from G451 to R450, D567, F575, F587, H609, E608, E588, N597, and back to G451. Thus, despite a total of 19 noncovalent interactions along the peptide chain from S384 to M645, a total of 104 grid sizes still resulted in an unusual higher systematic thermal instability (T_i) of 5.47 (Table 1). That may be the reason why the crystal X-ray structure of isolated hNBD1-Δ(RE, RI) is unavailable in the absence of Mg/ATP (28).

In addition to those intra-domain noncovalent interactions, there were also some noncovalent interactions between NBD1 and ICL4 (Figure 1b). These interactions included a salt bridge between E474 and R1066, an H-bond between E504 and Y1073, and seven π interactions such as M469-W1063, L1065-F1074-Y1073, F1068-F508-Y1073/F1074 and R1070-F508. Notably, F508, Y1073 and F1074 created the smallest triangle thermoring to stabilize the NBD1-ICL4 interface. In this case, it is necessary to examine whether these interfacial interactions affect the melting temperature threshold (T_m) of NBD1.

When D443 in the N-terminal region H-bonded with Y627 in the C-terminal region, the biggest $Grid_{21}$ structure was created (Figure 1c). It had a 21-residue size to govern the D443-Y627 H-bond via a thermoring from D443 to R450, D567, F575, F587, H609, E608, K612, H620, Y625, Y627, and back to D443 (Figure 1c-d). When sealed with 2.0 equivalent basic H-bonds, the calculated T_m was approximately 32 °C, matching the melting threshold of isolated hNBD1-Δ(RE, RI) measured by DSC (Table 1) (9). Consequently, the presence of stronger NBD1-ICL4 interactions may not increase the melting temperature threshold of NBD1 in the absence of bound Mg/ATP.

NBD1-NBD2 dimerization increases the melting threshold of hNBD1

When hCFTR is phosphorylated for Mg/ATP-dependent NBD1-NBD2 dimerization, the NBD1 (PDB, 6MSM) from E384 to Q637 exhibits a disordered segment from 638 to 646 with the unstructured RI shifting from 403-438 to 410-434 (16). Despite this minor alteration in the primary sequence structure, the tertiary noncovalent structure of NBD1 remains comparable to that of the isolated hNBD1-Δ(RE, RI) when bound by Mg/ATP for NBD dimerization (Figures 2a & S2) (30).

First, the Mg/ATP binding site remained intact. For instance, T465, Q493 and D572 formed a stable triangle via Mg^{2+}. Meanwhile, ATP connected W401, K464 and S466. Additionally, W401 engaged in a π interaction with L475. However, the T388-T390, S459-H620 and G486-D567 H-bonds, as well as the F446-Y627 and H484-L568 π interactions were disrupted. Instead, the E391-K447 H-bond and the M394-F446 and F400-F409 π interactions were observed.

Second, there were some noncovalent bridges present near F508. These included the W496-F508 and Y512-Y517 π interactions, as well as the Y512-E514, Y517-E537 and D529-Q552/R555 H-bonds. However, the W496-R560 and I507-Y563 π interactions, as well as the N505-R560 and R518-E527 H-bonds were replaced with the F508-R560, Y517-I521, and F533-I539 π interactions along with the S557-R560 H-bond. In addition, the H-bond between K503 and Y512 was found to be a π bridge.

Third, common noncovalent interactions were also observed near the Mg^{2+} site. For example, Y569-M595, P574-F575-F587-C592 and H609-F587/F575 π interactions, along with the R583-H609-T604 H-bonds. The only difference was that the D565-K598 salt bridge and the D579-T582 H-bond were substituted with the D579-E585 H-bond.

Fourth, in the C-terminal region only the F626-L633 π interaction and the T629-S631 H-bond were intact. The H620-F640-Y625 π interactions were absent, as well as the D639-S641/S642 H-bonds, but the Y625-Q637 H-bond appeared.

Most importantly, although most of the NBD1-ICL4 interactions were maintained upon R domain phosphorylation except for the replacement of the E574-Y1073 H-bond with the L1065-F1074 π interaction (Figure 2b), the biggest $Grid_{13}$ in the isolated hNBD1 was dissociated along with the broken F446-Y627 and S459-H620 bridges at the interface between the C- and N- termini. Instead, the biggest $Grid_8$ was present along with the least-stable Q525-E585 H-bond (Figure 2a). It had an 8-residue size to control the new H-bond via a thermoring from Q525, D529, R555, S557,

R560, F508, W496, Q493, Mg^{2+}, D572, P574, F575, F587, E585 and back to Q525 (Figures 2c-d). With 1.5 equivalent basic H-bonds sealing it, the calculated melting temperature threshold (T_m) was about 53 °C, higher than the melting threshold of 48 °C measured by DSC for isolated hNBD1-Δ(RE, RI) (Table 1) (9, 28). Meanwhile, the systematic thermal instability (T_i) dramatically decreased from 5.47 to 2.17 along with a total of 35 non-covalent bridges and 76 grid sizes (Table 1). Therefore, NBD1-NBD2 dimerization may enhance the thermal stability of NBD1 in the full-length phosphorylated hCFTR. Since F508 played a critical role in forming the biggest $Grid_8$, it is exciting to test if its deletion would affect the thermal stability of NBD1 in the presence of Trikafta.

NBD1-NBD2 dimerization also increases the melting threshold of (F508del)hNBD1 in Trikafta-bound hCFTR

When F508 was deleted to disrupt the W496-F508-R560 π interactions, in the presence of Trikafta, the biggest $Grid_8$ was dissociated. This caused the disruption of the Q525-E585 H-bond and the shift of the S557-R560 H-bond to the N505-R560 one (Figures 3a & S3). As a result, the H-bond moved from E391-K447 to N396-D443 near the same Mg/ATP site along with a new salt bridge between R487 and D567, a new H-bond between E449 and Q452, and a new π interaction between F446 and L454. When this conformational change transmitted to the C-terminal region, the T604-H609, Y625-Q637 and T629-S631 H-bonds along with the F626-L633 π interaction were disconnected. Meanwhile, a new E608-K611 salt bridge, a new T629-E632 H-bond and new K611-F630 and H620-Y625 π interactions were produced. Overall, although the total number of noncovalent interactions decreased from 35 to 34 along the peptide chain from E391 to Q637, the total grid sizes increased from 76 to 83 (Figure 3a). Thus, the systematic thermal instability (Ti) still increased from 2.17 to 2.44 (Table 1).

On the other hand, the removal of F508 also disrupted most of the NBD1-ICL4 interactions except for the M469-W1063 π interaction. In addition, the E474-R1066 H-bond was replaced with the Y380-R1066 π interaction (Figure 3b). Despite these weakened interfacial interactions between NBD1 and ICL4, the biggest $Grid_{12}$ was present in the C-terminal region. With a 12-residue size to control the least-stable K611-F630 π interaction which was equivalent to 1.5 basic H-bonds, the calculated melting threshold for the thermoring from K611 to H620, Y625, F630, and back to K611 was about 45 °C higher than the melting threshold of 40 °C measured by DSC

(Table 1) (9). Hence, the NBD1-NBD2 dimerization also increased the melting threshold in the presence of Trikafta. Since the broken D443-T627 H-bond was found for Mg/ATP-mediated NBD dimerization, the release of the C-terminal region from NBD1 was necessary. The question is how Trikafta achieves this when binding to TMD1 and TMD2, rather than NBD1 or the NBD1-NBD2 interface or the NBD1-ICL4 interface.

Tight TMD1-TMD2 interactions at the gating center are required for CFTR opening

Our previous study showed that K190 and K978 are located in the tetrahelix bundle of hCFTR. Constitutive gain of function (GOF) mutations such as K978C and K190C significantly stimulate ATP-independent but PKA-dependent channel activation, thereby increasing ATP and PKA sensitivity allosterically. Importantly, these constitutive ICL mutations can restore the function of CFTR mutants like G551D without ATP binding and NBD2-free Δ1198 without NBD dimerization (31). They also prevent the irreversible thermal inactivation of ΔF508 hCFTR (10). All of this suggests that the tetrahelix bundle acts as a critical gating center for ATP-independent but phosphorylation-dependent CFTR activation.

Given that the extracellular gate remains closed in a cryo-EM structure of zebrafish CFTR (zCFTR) even after R domain phosphorylation and ATP binding (32), this structure can serve as an ideal negative control to investigate how the tetrahelix bundle gates the CFTR channel in an ATP-independent manner.

In the dephosphorylated closed state of wild type (WT) hCFTR, the segment 970-985 in TM9 was structured as a α-helix and connected with TM4 via the R251-D985 H-bond. R251 and S256 in TM4 were located on two separated α-helices. Similarly, T1053 and E1046 in TM10 were also positioned on two separated α-helices. The C-terminal region of the R domain was wedged among TMs 3, 4, 9, and 10 (Figure 4a). This is reminiscent of the inhibitory lipid at the active vanilloid site in heat-gated transient receptor potential vanilloid-1 (TRPV1) or 3 (TRPV3) bio-thermometers (33-34).

When phosphorylation released the R domain for channel opening, both TM4 and TM10 underwent a π-to-α transition. In addition to the R251-D985 H-bond, R1048 also formed H-bonds with both N974 and D979 via their side chains, leading to a smaller $Grid_4$. Meanwhile, N189 H-bonded with E1044, F976 formed a CH-π interaction with T262, and Q179 H-bonded with S256 via their side chains. However, T1053 H-bonded with the backbone NH at G970. Notably, K1060 linked with E267 via an H-bond, confirming the previous report (Figure 4a) (35).

In contrast, the R domain between TMD1 and TMD2 in zCFTR was found to be unstructured in the dephosphorylated closed state (36). This state also included a salt bridge between K252 (R251 in hCFTR) and D993 (D985 in hCFTR), as well as an H-bond between N982 and R983 (N974 and R975 in CFTR). In addition, Q180 and G190 were separated by two α-helices in TM3. Finally, both the segment 978-979 in TM9 and the segment E1052-R1056 in TM10 displayed a loose α-helix (Figure 4b).

In the presence of Mg/ATP agonists that stimulate the phosphorylated zCFTR, the loose α-helix in TM9 extended to D987 (D979 in hCFTR), and the segment E1052-R1056 in TM10 restored its α-helix. In this case, most noncovalent interactions were disrupted, including the D987-R1056-N982 (D979-R1048-N974 in hCFTR) H-bonds and the F984-T263 (F976-T262 in hCFTR) π interaction. Instead, only the E1052-R1056, R979-E1054 and G978-S1061 H-bonds were present in this inactivated state despite the presence of the well-known R554-T1247 (R555-T1246) H-bond (32) (Figure 4b). Therefore, the tetrahelix bundle acts as a pivotal gating center and tight TMD1-TMD2 interactions at this center are required for CFTR activation.

Trifafta tightens TMD1-TMD2 interactions at the gating center to release the phosphorylated R domain

Since there is no crack between TMD1 and TMD2 of phosphorylated ΔF508-hCFTR upon Trikafta and Mg/ATP binding (22), it is necessary to examine if Trikafta activates the gating center. The study on the tertiary structure of this activated mutant indicated that despite the disruption of the F976-T262 π interaction and the Q179-S256 and E267-K1060 H-bonds, TM10 exhibited two α–helices at the T1053-E1046 interface. This allowed for new R975-E1046 and E1044-N186 H-bonds at the TM9-TM10-TM3 interface. Thus, a much smaller $Grid_1$ produced a more thermally stable triangle among N974, R975, E1046, and R1048 (Figure 5a). Since VX-809 alone stimulates ΔF508-CFTR activity in the absence of structured NBD1 (22, 26), the gating defect of ΔF508-hCFTR was first rescued upon activation of the gating center before ATP-medicated NBD1-NBD2 dimerization.

Further detailed studies showed that all three modulators in Trikafta work together to enhance this unique H-bond network via their noncovalent interactions with TMD1 and TMD2. For example, tezacaftor (VX-661) connected R74, F78, and F81 from TM1, H199 from TM3, and W361 from TM6. In addition, ivacaftor (VX-770) bridged F236 from TM4 with Y304, F305,

S308 and F312 from TM5 and F931 from TM8. These two modulators promoted the formation of the N189-E1044 H-bond (data not shown). Finally, elexacaftor (VX-445) linked S18 from the lasso motif, Y1032 from TM10, and W1098 and R1102 from TM11 (Figure 5a). This dual modulator also added the R975-E1046 H-bond (Figure 5a). Together, after Trikafta binding to activate the gating center, tight TMD1-TMD2 interactions allowed the robust H-bonding network to outcompet the R domain from the TMD1-TMD2 interface. This is reminiscent of the release of lipid from the active vanilloid site of TRPV3 upon the binding of 2-aminoethoxydiphenyl borate (2-APB) near the site (37).

Tight TMD1-TMD2 interactions at the gating center allows the phosphorylated S813 site to link the ICL1-ICL4 interface with the N-and C-terminal tails of TMD1

A recent cryo-EM structure indicated that when the PKA catalytic subunit (PKA-C) stabilizes the open state of phosphorylated hCFTR, the phosphate group of S813 is sandwiched between R487/K564 of NBD1 and R1070 of TMD2 at the NBD1/ICL4 interface (38). Due to the similar TMD1-TMD2 interactions at the gating center in this PKA-C-activated hCFTR (data not shown), it is essential to investigate if the phosphorylated S813 site of ΔF508 hCFTR also interacts with both NBD1 and TMD2 once Trikafta tightens TMD1-TMD2 interactions at the gating center.

The molecular docking investigation revealed that the phosphate group of S813 was unable to form a salt bridge with R487 and K564 of NBD1 or R1070 of TMD2. Instead, it was positioned between K162 and K166 at ICL1 while Y808 was found to engage in putative strong π–π interactions with R1066 at ICL4 and Y380 at the TMD1-NBD1 linker or the C-terminal tail of TMD1. More importantly, R811 H-bonded with E54 and D58 at the N-terminal tail of TMD1 (Figure 5b). This model may account for why the E54A or D58A or E54A/D58A mutation inhibits the binding of the R domain to the N-terminal tail and the related hCFTR activity (39), and why mutations such as K166A/H, R1066H, S813D/Y808A and S813D/R811A suppress curcumin potentiation (40). Notably, curcumin can also stabilize the random, competitive and stimulatory binding of the phosphorylated S795 site to these interfaces (40). That is why curcumin is not effective in maintaining ΔF508 CFTR activity at room temperature (41), or preventing the irreversible thermal inactivation of ΔF508-hCFTR at physiological temperature (10). On the other hand, since Trikafta modulators maintain the higher ΔF508-hCFTR activity even at physiological temperature of 37 °C (23-27), it is suggested that the specific interactions of the phosphorylated

S813 site with not only the ICL1-ICL4 interface but also the N- and C-terminal tails of NBD1 be necessary to release the C-terminal region from NBD1 for ATP-mediated dimerization with NBD2.

Release of the C-terminal region from NBD1 allows tight NBD dimerization to stabilize NBD1

In the dephosphorylated hCFTR, the R domain separates NBD1 from NBD2. In that case, similar to the D529-Q552 H-bond in NBD1, D1377 also H-bonded with T1380 in NBD2 (Figure 6). However, in the phosphorylated state, the release of the C-terminal region from NBD1 allowed for tight dimerization with NBD2.

A previous study demonstrated that two isolated NBD1 peptides can form a head-to-tail homodimer in the presence of Mg/ATP when the RE and RI regions are deleted (28). However, the noncovalent interactions between two NBD1 peptides are limited to the Mg/ATP site. On one side of the interface, the Walker A half-site shows extensive interactions along the phosphates, Mg^{2+} and the Walker A residues such as K464, T465 and S466. On the other side, the signature LSGGQ half-site also interacts with the phosphates through H-bonds (28).

However, when NBD1 and NBD2 dimerized, more noncovalent interactions were found between them regardless of the presence of F508 and Trikafta. In addition to the traditional interactions between the phosphates and the Walker A/B half-site or the signature LSHGH/ LSGGQ half-site, some new noncovalent interactions were also observed nearby (Figure 6). For example, the D529-R1245 and R555-T1246 H-bonds near the Walker A half-site and the T460-T1380 H-bond near the Walker B half-site. More importantly, Y577 from NBD1 formed a strong π–π interaction with H1375 from NBD2. In that regard, it is reasonable that NBD1 was stabilized along with the increased melting temperature thresholds, 53 °C for wtCFTR and 45 °C for ΔF508-CFTR (Table 1).

DISCUSSION

F508 in NBD1, like F251 in β-D-glucoside glucohydrolase (42), plays a central role in CFTR expression on the cell surface and ATP/PKA-mediated channel activity. The deletion of F508 (ΔF508) on the surface of NBD1 destabilizes NBD1 and the nearby interdomain interactions, leading to both thermal and gating defects (17-21). Thus, rescuing strategies have focused on this domain and its interfaces (20, 43-47). Although Trikafta modulators do not target them, they successfully correct both defects of phosphorylated ΔF508-hCFTR even at 37 °C along a significantly different pathway (23-27). This study demonstrated that the specific noncovalent

interactions of the phosphorylated S813 site with ICL1, ICL4, and N-/C- terminal tails of TMD1 upon Trikafta-triggered tight TMD1-TMD2 interactions at the gating center played a pivotal role in rescuing ΔF508-CFTR. Although the deletion of F508 causes the primary thermal defect in NBD1 and then the gating defect at the gating center, Trikafta rescued them in a reverse manner allosterically.

Our previous studies revealed the role of constitutive mutations K190C and K978C at the gating center in ATP-independent but phosphorylation-dependent hCFTR activation (10), and the E267-K1060 salt-bridge at this center allosterically couples to R domain phosphorylation (35). This study further indicated a strong H-bonding network from G970 to D985 rather than this salt bridge, linking TMs 3, 4, 9 and 10 together to favor releasing the R domain from the gating center for channel opening (Figure 4). Thus, either the constitutive mutations such as K190C and K978C or Trikafta may enhance this H-bonding network for ATP-independent but phosphorylation-dependent channel activation. Since this gating center is surrounded by TMD1/2 and NBD1/2 at the protein-water interface, it may also serve as a stabilization center for thermo-stability and thermo-activity (48). Similar to lysine ligation to the heme iron in cytochrome c (49), remote perturbations at this gating center by Trikafta can allosterically regulate ATP binding for NBD dimerization. Furthermore, the phosphorylated or unphosphorylated R domain can act as a global regulator of CFTR via its alternative random interacting partners such as the C-terminal region of CFTR (50), ICL3 (51-54) that inhibits channel opening even in the presence of ATP-mediated NBD1-NBD2 dimerization (51), or the ICL1-ICL4 interface which can be strengthened by curcumin to stabilize the open state (40, 55). Hence, although curcumin and Trikafta have different targets (56), the complete release of the R domain from the TMD1-TMD2 interface by the interdomain H-bonding network at the gating center may facilitate its stimulatory binding to the ICL1-ICL4 interface (Figures 4a & 5), allowing for ATP-independent channel opening and subsequent ATP-mediated NBD1-NBD2 dimerization via global rewiring inter-domain allosteric-networks (21-22, 57). In support of this proposal, the dephosphorylated R domain was also found as a hairpin loop between TMD1 and TMD2 of the glutathione transporter Yeast Cadmium Factor 1 (Ycf1) E1435Q mutant (58). However, the phosphorylated R domain as found near the ICL1-ICL4 interface of the open E1371Q-hCFTR or the Ycf1 E1435Q mutant (16, 59), disappeared upon Trikafta binding (22). Further, when PKA stabilizes the open state (38), the phosphate group of S813 fills the cavity at the NBD1/TMD interface through salt bridges with R487 and K564 of

NBD1, as well as R1070 of TMD2 (38). Thus, despite of the weakened NBD1-ICL4 interactions in ΔF508 CFTR, once the gating defect at the gating center was rescued by Trikafta-induced tight TMD1-TMD2 interactions, the complete release of the phosphorylated R domain allowed its specific electrostatic interactions of the phosphate group at 813 with K166 at ICL1, the specific π interactions of Y808 with Y380 at the TMD1-NBD1 linker and R1066 at ICL4, and the specific H-binding of R811 with E54 and D58 at the N-terminal tail of TMD1 (Figure 5b). As a result, the C-terminal region could be released from NBD1 in favour of ATP-medicated tight NBD1-NBD2 dimerization, which stabilized NBD1 to stop irreversible thermal inactivation (10, 12). Based on this important role of this interdomain H-bonding network at the gating center, it is reasonable to find some CF-causing mutations G970E/D, D979V, E1044X, E1046X, and T1053I are located at this gating center (http://www.genet.sickkids.on.ca/cftr; https://cftr2.org).

A recent study on isolated hNBD1 revealed that the melting temperature threshold of hNBD1 is determined by the C-terminal region, which is closely related to the least-stable noncovalent interaction in the biggest thermoring (30). In the full-length hNBD1 and (F508del)hNBD1 monomers, the S605-R658 H-bond in the biggest $Grid_{16}$ and $Grid_{20}$ controls the matched melting thresholds of 37 °C and 29 °C, respectively. The deletion of RE and RI allows for Mg/ATP-mediated NBD1-NBD1 dimerization. In that case, the F446-Y627 and S459-H620 noncovalent bridges in the biggest $Grid_{13}$ governs the matched melting threshold of 48 °C for isolated hNBD1-Δ(RE, RI). When F508 is deleted, only the F446-Y627 π bridge in the biggest $Grid_{17}$ sets the matched melting threshold of 40 °C. In any case, the F446-Y627 π bridge is still present between the C- and N-termini. That may be the reason why isolated hNBD1-Δ(RE, RI) cannot dimerize with NBD2 (28).

This study further indicated that the biggest $Grid_{21}$ had a matched melting threshold of 32 °C to control the least-stable D443-Y627 H-bond in NBD1 of dephosphorylated hCFTR even in the presence of tight NBD1-ICL4 interactions (Figures 1 & 7, Table 1). In contrast, no noncovalent interaction was present between the C- and N-termini when the channel with or without F508 is phosphorylated by PKA for Mg/ATP-dependent NBD1-NBD2 dimerization (Figures 2, 3 & 7). Therefore, the C-terminal region must be released from NBD1 for ATP-dependent NBD1-NBD2 dimerization, which in turn increased the melting threshold of NBD1, thereby stabilizing NBD1. For the E1371Q mutant, the Q525-E585 H-bond in the biggest $Grid_8$ determined the melting threshold of NBD1 up to 53 °C (Figure 2, Table 1). Even if F508 is deleted, the presence of

Trikafta still allowed the K611-F630 bridge in the biggest $Grid_{12}$ to maintain the higher melting threshold of 48 °C (Figure 3, Table 1). Taken together, Trikafta binding to TMD1 and TMD2 triggered a series of tight interdomain interactions around the gating center, rescuing both gating and thermal defects of ΔF508 allosterically at physiological temperature.

CONCLUSIONS

The thermoring analysis has been used to identify the thermodynamic signature for the melting threshold of a protein. This study further demonstrated that it can define the interdomain interaction that stabilizes the flexible conformation of an active domain within a complex full-length membrane protein with multiple domains. Further, similar to the active role of the lipid-dependent vanilloid site in heat-evoked channel activation of TRPV1 or TRPV3, the R domain-dependent gating center at both TMD1-TMD2 and NBD1-NBD2 interfaces may play an essential role in correcting both gating and thermal defects caused by cystic fibrosis mutations. Thus, a drug could target a remote site in one domain to rescue the thermal and gating defects induced by a missense mutation in the other domain allosterically,

COMPUTATIONAL METHODS

Data mining resources

Three cryo-EM structures of human CFTR (hCFTR) constructs with or without F508 at 4 °C were chosen for thermoring analysis. These structures included dephosphorylated hCFTR in a closed state (PDB ID, 5UAK, model resolution = 3.87 Å) (14), phosphorylated E1371Q with Mg/ATP bound in an open state (PDB ID, 6MSM, model resolution = 3.2 Å) (16), and phosphorylated hCFTR/E1371Q/ΔF508 with Mg/ATP/Trikafta bound in an open state (PDB ID, 8EIQ, model resolution = 3.0 Å) (22). Additionaly, cryo-EM structures of zebrafish CFTR (zCFTR) constructs with and without phosphorylation and Mg/ATP bound (PDB, 5W81 and 5TSI, model resolutions 3.4 Å and 3.7 Å respectively) were used as controls to indicate the role of the gating center (32, 36). Finally, the cryo-EM structure of phosphorylated hCFTR with Mg/ATP/PKA-C bound (PDB, 9DW9, model resolution = 2.8 Å) was also used to fit the phosphorylated S813 site to the ICL1-ICL4 interface (38).

Standard methods for filtering non-covalent interactions

The standard methods for filtering non-covalent interactions, along with exact calculations, were the same as those previously used, ensuring accurate and repeatable results (30, 33-34, 60-64). UCSF Chimera was used to review potential stereo-selective or regio-selective intra-domain lateral noncovalent interactions along the single peptide chain of hNBD1 with or without F508. These interactions included salt bridges, H-bonds and lone pair/CH/cation-π interactions between paired amino acid side chains. When a backbone NH at a residue position was within a cutoff distance for an H-bond with a side chain of a nearby residue, that H-bond was also considered. Detailed cutoff distances and interaction angles can be obtained in the online Supporting Information (Tables S1, S2, and S3). In this study, approximately at least 19 different noncovalent interactions were identified along the single peptide chain from L383 to Q637 on each protomer.

Calculations based on the thermoring structures and the grid thermodynamic model

The tertiary thermoring structure of NBD1 was based on a noncovalently-interacting network, where amino acid residues served as nodes, and links represented noncovalent interactions between two residues. Since noncovalent interactions are undirected, each link had the shortest round path (geodesic transportation distance) from a specific residue back to the same one. It consisted of the shortest direct and reverse network paths between two nodes. The direct path defined as the link itself had a length of zero due to no free residue within a noncovalent interaction. Thus, the shortest reverse network path included the segment of the polypeptide chain and other noncovalent interactions than the link. Based on the Floyd algorithm (65), its length was constrained as the minimal total number of free or silent side chains of residues not involved in any noncovalent interactions along this path. According to the established grid thermodynamic model (30, 33-34, 60-64), each shortest round path formed a thermoring or grid to control the least-stable noncovalent interaction. Once the biggest grid was identified, the least-stable noncovalent interaction along the peptide chain could be determined to calculate a melting temperature threshold using the following equation as examined previously (30, 33-34, 60-64):

$$T_m\,(°C) = 34 + (n - 2) \times 10 + (20 - s) \times 2 \qquad (1)$$

where, n represents the total number of basic H-bonds (each approximately 1 kcal/mol) equivalent to the least-stable noncovalent interaction controlled by the given grid; and s is the grid size used to control the least-stable noncovalent interaction within the grid.

Additionally, the total grid sizes (S) and the total non-covalent interactions (N) along the same polypeptide chain could be utilized to calculate grid-based systematic thermal instability (T_i) using the same equation as examined previously (30, 33-34, 60-64):

$$T_i = S/N \tag{2}$$

This calculation allows for the assessment of the peptide's compact conformational entropy.

ABBREVIATIONS

ABC, ATP-binding cassette

CF, cystic fibrosis

cryo-EM, cryoelectron microscopy

CFTR, cystic fibrosis transmembrane conductance regulator

DSC, differential scanning calorimetry

DSF, differential scanning fluorimetry

GOF, gain of function

hCFTR, human CFTR

ICL1, intracellular loop 1

ICL4, intracellular loop 4

NBD1, nucleotide binding domain 1

NBD2, nucleotide binding domain 2

PKA, protein kinase A

PKA-C, the PKA catalytic subunit

R, regulatory

RE, regulatory extension

RI, regulatory insert

T_i, systematic thermal instability

T_m, melting temperature threshold

TMH, transmembrane helix

TMD1, transmembrane domain 1

TMD2, transmembrane domain 2

TRPV1, transient receptor potential vanilloid-1

TRPV3, transient receptor potential vanilloid-3

2-APB, 2-aminoethoxydiphenyl borate

WT, wild type

wtCFTR, wild type CFTR

Ycf1, Yeast Cadmium Factor 1

zCFTR, zebrafish CFTR

REFERENCES

1. Riordan JR, Rommens JM, Kerem B, Alon N, Rozmahel R, Grzelczak Z, Zielenski J, Lok S, Plavsic N, Chou JL, et al. Identification of the cystic fibrosis gene: cloning and characterization of complementary DNA. *Science*. **245,** 1066-1073 (1989).
2. Anderson MP, Berger HA, Rich DP, Gregory RJ, Smith AE, Welsh MJ. Nucleoside triphosphates are required to open the CFTR chloride channel. *Cell*. **67**, 775-84. (1991).
3. Anderson MP, Gregory RJ, Thompson S, Souza DW, Paul S, Mulligan RC, Smith AE, Welsh MJ. Demonstration that CFTR is a chloride channel by alteration of its anion selectivity. *Science*. **253**, 202-5 (1991).
4. Meng X, Clews J, Kargas V, Wang X, Ford RC. The cystic fibrosis transmembrane conductance regulator (CFTR) and its stability. *Cell Mol Life Sci.* **74**, 23-38 (2017).
5. Kerem B, Rommens JM, Buchanan JA, Markiewicz D, Cox TK, Chakravarti A, Buchwald M, Tsui LC. Identification of the cystic fibrosis gene: genetic analysis. *Science.* **245**, 1073-80 (1989).
6. Dalemans W, Barbry P, Champigny G, Jallat S, Dott K, Dreyer D, Crystal RG, Pavirani A, Lecocq JP, Lazdunski M. Altered chloride ion channel kinetics associated with the delta F508 cystic fibrosis mutation. *Nature* **354,** 526–528 (1991).
7. Lukacs GL, Chang XB, Bear C, Kartner N, Mohamed A, Riordan JR, Grinstein S. The delta F508 mutation decreases the stability of cystic fibrosis transmembrane conductance regulator in the plasma membrane. Determination of functional half-lives on transfected cells. *J Biol Chem*. **268**, 21592-8 (1993).
8. Sharma M, Benharouga M, Hu W, Lukacs GL. Conformational and temperature-sensitive stability defects of the delta F508 cystic fibrosis transmembrane conductance regulator in post-endoplasmic reticulum compartments. *J Biol Chem.* **276**, 8942-50 (2001).
9. Protasevich I, Yang Z, Wang C, Atwell S, Zhao X, Emtage S, Wetmore D, Hunt JF, Brouillette CG. Thermal unfolding studies show the disease causing F508del mutation in CFTR thermodynamically destabilizes nucleotide-binding domain 1. *Protein Sci.* **19,** 1917-1931 (2010).
10. Wang W, Okeyo GO, Tao B, Hong JS, Kirk KL. Thermally unstable gating of the most common cystic fibrosis mutant channel (ΔF508): "rescue" by suppressor mutations in

nucleotide binding domain 1 and by constitutive mutations in the cytosolic loops. *J Biol Chem.* **286**, 41937-41948 (2011).

11. Rabeh WM, Bossard F, Xu H, Okiyoneda T, Bagdany M, Mulvihill CM, Du K, di Bernardo S, Liu Y, Konermann L, Roldan A, Lukacs GL. Correction of both NBD1 energetics and domain interface is required to restore ΔF508 CFTR folding and function. *Cell*. **148**,150-163 (2012).
12. Liu X, Dawson DC. Cystic fibrosis transmembrane conductance regulator (CFTR) potentiators protect G551D but not ΔF508 CFTR from thermal instability. *Biochemistry*. **53**, 5613-8 (2014).
13. Froux L, Coraux C, Sage E, Becq F. Short-term consequences of F508del-CFTR thermal instability on CFTR-dependent transepithelial currents in human airway epithelial cells. *Sci Rep.* **9**,13729 (2019).
14. Liu F, Zhang Z, Csanády L, Gadsby DC, Chen J. Molecular Structure of the Human CFTR Ion Channel. *Cell*. **169,** 85-95.e8 (2017).
15. Vergani P, Lockless SW, Nairn AC, Gadsby DC. CFTR channel opening by ATP-driven tight dimerization of its nucleotide-binding domains. *Nature* **433**, 876-80 (2005).
16. Zhang Z, Liu F, Chen J. Molecular structure of the ATP-bound, phosphorylated human CFTR. *Proc Natl Acad Sci U S A.* **115,** 12757-12762 (2018).
17. Du K, Sharma M, Lukacs GL. The DeltaF508 cystic fibrosis mutation impairs domain-domain interactions and arrests post-translational folding of CFTR. *Nat Struct Mol Biol.* **12**, 17-25 (2005).
18. Cui L, Aleksandrov L, Chang XB, Hou YX, He L, Hegedus T, Gentzsch M, Aleksandrov A, Balch WE, Riordan JR. Domain interdependence in the biosynthetic assembly of CFTR. *J Mol Biol* **365**, 981–994 (2007).
19. Jih KY, Li M, Hwang TC, Bompadre SG. The most common cystic fibrosis-associated mutation destabilizes the dimeric state of the nucleotide-binding domains of CFTR. *J Physiol.* **589**(Pt 11), 2719-31 (2011).
20. He L, Aleksandrov AA, An J, Cui L, Yang Z, Brouillette CG, Riordan JR. Restoration of NBD1 thermal stability is necessary and sufficient to correct ΔF508 CFTR folding and assembly. *J Mol Biol.* **427**, 106-20. (2015)
21. Soya N, Xu H, Roldan A, Yang Z, Ye H, Jiang F, Premchandar A, Veit G, Cole SPC, Kappes J, Hegedüs T, Lukacs GL. Folding correctors can restore CFTR posttranslational folding landscape by allosteric domain-domain coupling. *Nat Commun.* **14**, 6868. (2023)

22. Fiedorczuk K, Chen J. Molecular structures reveal synergistic rescue of Δ508 CFTR by Trikafta modulators. *Science*. **378**, 284-290 (2022).
23. Keating D, Marigowda G, Burr L, Daines C, Mall MA, McKone EF, Ramsey BW, Rowe SM, Sass LA, Tullis E, McKee CM, Moskowitz SM, Robertson S, Savage J, Simard C, Van Goor F, Waltz D, Xuan F, Young T, Taylor-Cousar JL; VX16-445-001 Study Group. VX-445-Tezacaftor-Ivacaftor in Patients with Cystic Fibrosis and One or Two Phe508del Alleles. *N Engl J Med.* **379**, 1612-1620 (2018).
24. Middleton PG, Mall MA, Dřevínek P, Lands LC, McKone EF, Polineni D, Ramsey BW, Taylor-Cousar JL, Tullis E, Vermeulen F, Marigowda G, McKee CM, Moskowitz SM, Nair N, Savage J, Simard C, Tian S, Waltz D, Xuan F, Rowe SM, Jain R; VX17-445-102 Study Group. Elexacaftor-Tezacaftor-Ivacaftor for Cystic Fibrosis with a Single Phe508del Allele. *N Engl J Med.* **381**,1809-1819 (2019).
25. Bose SJ, Bijvelds MJC, Wang Y, Liu J, Cai Z, Bot AGM, de Jonge HR, Sheppard DN. Differential thermostability and response to cystic fibrosis transmembrane conductance regulator potentiators of human and mouse F508del-CFTR. *Am J Physiol Lung Cell Mol Physiol.* **317**, L71-L86 (2019).
26. Veit G, Roldan A, Hancock MA, Da Fonte DF, Xu H, Hussein M, Frenkiel S, Matouk E, Velkov T, Lukacs GL. Allosteric folding correction of F508del and rare CFTR mutants by elexacaftor-tezacaftor-ivacaftor (Trikafta) combination. *JCI Insight.* 5, e139983. (2020).
27. Veit G, Vaccarin C, Lukacs GL. Elexacaftor co-potentiates the activity of F508del and gating mutants of CFTR. *J Cyst Fibros*. **20**, 895-898 (2021).
28. Atwell S, Brouillette CG, Conners K, Emtage S, Gheyi T, Guggino WB, Hendle J, Hunt JF, Lewis HA, Lu F, Protasevich II, Rodgers LA, Romero R, Wasserman SR, Weber PC, Wetmore D, Zhang FF, Zhao X. Structures of a minimal human CFTR first nucleotide-binding domain as a monomer, head-to-tail homodimer, and pathogenic mutant. *Protein Eng Des Sel.* **23,** 375-384 (2010).
29. Soya N, Roldan A, Lukacs GL. Differential Scanning Fluorimetry and Hydrogen Deuterium Exchange Mass Spectrometry to Monitor the Conformational Dynamics of NBD1 in Cystic Fibrosis. *Methods Mol Biol*. **1873**, 53-67 (2019).
30. Wang G. ATP-dependent thermoring basis for the heat unfolding of the first nucleotide-binding domain isolated from CFTR. *Research Square* (in production, 2024).

31. Wang W, Wu J, Bernard K, Li G, Wang G, Bevensee MO, Kirk KL. ATP-independent CFTR channel gating and allosteric modulation by phosphorylation. *Proc Natl Acad Sci U S A.* **107**, 3888-3893 (2010).
32. Zhang Z, Liu F, Chen J. Conformational Changes of CFTR upon Phosphorylation and ATP Binding. Cell. **170**, 483-491.e8 (2017).
33. Wang G. Thermoring-Based Heat Activation Switches in the TRPV1 Biothermometer. *Int. J. Biol. Macromol.* **248,** 125915 (2023).
34. Wang G. Thermoring basis for the TRPV3 bio-thermometer. *Sci Rep.* **13,** 21594 (2023).
35. Wang W, Roessler BC, Kirk KL. An electrostatic interaction at the tetrahelix bundle promotes phosphorylation-dependent cystic fibrosis transmembrane conductance regulator (CFTR) channel opening. *J Biol Chem.* **289**, 30364-30378 (2014).
36. Zhang Z, Chen J. Atomic Structure of the Cystic Fibrosis Transmembrane Conductance Regulator. *Cell*. **167**,1586-1597.e9 (2016).
37. Nadezhdin K. D., Neuberger A., Khosrof L. S., Talyzina I. A., Khau J., Yelshanskaya M. V., Sobolevsky A. I. TRPV3 activation by different agonists accompanied by lipid dissociation from the vanilloid site. *Sci Adv.* **10**, eadn2453 (2024).
38. Fiedorczuk K, Iordanov I, Mihályi C, Szöll} osi A, Csanády L, Chen J (2024) The structures of protein kinase A in complex with CFTR: Mechanisms of phosphorylation and reversible activation. *Proc Natl Acad Sci USA* **121,** e2409049121 (2024).
39. Naren AP, Cormet-Boyaka E, Fu J, Villain M, Blalock JE, Quick MW, Kirk KL. CFTR chloride channel regulation by an interdomain interaction. *Science.* **286**, 544-8 (1999).
40. Wang G. Molecular Basis for Fe(III)-Independent Curcumin Potentiation of Cystic Fibrosis Transmembrane Conductance Regulator Activity. *Biochemistry.* **54,** 2828-2840. Erratum in: *Biochemistry*. **54**, 4161 (2015).
41. Wang W, Li G, Clancy JP, Kirk KL. Activating cystic fibrosis transmembrane conductance regulator channels with pore blocker analogs. *J Biol Chem.* Jun 24;280(25):23622-30 (2005).
42. Souza VP, Ikegami CM, Arantes GM, Marana SR. Protein thermal denaturation is modulated by central residues in the protein structure network. *FEBS J.* **283**, 1124-38 (2016).
43. Sampson HM, Robert R, Liao J, Matthes E, Carlile GW, Hanrahan JW, Thomas DY. Identification of a NBD1-binding pharmacological chaperone that corrects the trafficking defect of F508del-CFTR. *Chem Biol.* **18**, 231-42 (2011).

44. Hall JD, Wang H, Byrnes LJ, Shanker S, Wang K, Efremov IV, Chong PA, Forman-Kay JD, Aulabaugh AE. Binding screen for cystic fibrosis transmembrane conductance regulator correctors finds new chemical matter and yields insights into cystic fibrosis therapeutic strategy. *Protein Sci.* **25**, 360-373 (2016).
45. Ehrhardt A, Chung WJ, Pyle LC, Wang W, Nowotarski K, Mulvihill CM, Ramjeesingh M, Hong J, Velu SE, Lewis HA, Atwell S, Aller S, Bear CE, Lukacs GL, Kirk KL, Sorscher EJ. Channel Gating Regulation by the Cystic Fibrosis Transmembrane Conductance Regulator (CFTR) First Cytosolic Loop. *J Biol Chem.* **291**, 1854-1865 (2016).
46. Carlile GW, Yang Q, Matthes E, Liao J, Radinovic S, Miyamoto C, Robert R, Hanrahan JW, Thomas DY. A novel triple combination of pharmacological chaperones improves F508del-CFTR correction. *Sci Rep.* **8**, 11404 (2018).
47. Padányi R, Farkas B, Tordai H, Kiss B, Grubmüller H, Soya N, Lukács GL, Kellermayer M, Hegedűs T. Nanomechanics combined with HDX reveals allosteric drug binding sites of CFTR NBD1. *Comput Struct Biotechnol J.* **20**, 2587-2599 (2022).
48. Magyar C, Gromiha MM, Sávoly Z, Simon I. The role of stabilization centers in protein thermal stability. *Biochem Biophys Res Commun*. **471**, 57-62 (2016).
49. Gu J, Shin DW, Pletneva EV. Remote Perturbations in Tertiary Contacts Trigger Ligation of Lysine to the Heme Iron in Cytochrome c. *Biochemistry.* **56**, 2950-2966 (2017).
50. Bozoky Z, Krzeminski M, Muhandiram R, Birtley JR, Al-Zahrani A, Thomas PJ, Frizzell RA, Ford RC, Forman-Kay JD. Regulatory R region of the CFTR chloride channel is a dynamic integrator of phospho-dependent intra- and intermolecular interactions. *Proc Natl Acad Sci USA* **110,** E4427–E4436 (2013).
51. Wang G State-dependent regulation of cystic fibrosis transmembrane conductance regulator (CFTR) gating by a high affinity Fe^{3+} bridge between the regulatory domain and cytoplasmic loop 3. *J Biol Chem* **285**, 40438-40447 (2010).
52. Wang G The inhibition mechanism of non-phosphorylated S768 in the R domain of CFTR. *J Biol Chem* **286**, 2171-2182. (2011)
53. Wang G and Duan D.D. Regulation of activation and processing of the cystic fibrosis transmembrane conductance regulator (CFTR) by a complex electrostatic interaction between the regulatory domain and cytoplasmic Loop 3. *J Biol Chem* **287**, 40484-40492. (2012).

54. Wang G. Interplay between inhibitory ferric and stimulatory curcumin regulates phosphorylation-dependent human cystic fibrosis transmembrane conductance regulator and ΔF508 activity. *Biochemistry* **54**, 1558-1566 (2015).
55. Wang G, Linsley R, Norimatsu Y. External Zn^{2+} binding to cysteine-substituted cystic fibrosis transmembrane conductance regulator constructs regulates channel gating and curcumin potentiation. *FEBS J.* **283,** 2458-2475 (2016).
56. Wang W, Hong JS, Rab A, Sorscher EJ, Kirk KL. Robust Stimulation of W1282X-CFTR Channel Activity by a Combination of Allosteric Modulators. *PLoS One.* **11**, e0152232 (2016).
57. Levring J, Terry DS, Kilic Z, Fitzgerald G, Blanchard SC, Chen J. CFTR function, pathology and pharmacology at single-molecule resolution. *Nature*. 616, 606-614 (2023). Erratum in: *Nature*. **617**, E11 (2023).
58. Khandelwal NK, Tomasiak TM. Structural basis for autoinhibition by the dephosphorylated regulatory domain of Ycf1. *Nat Commun.* **15**, 2389 (2024).
59. Khandelwal NK, Millan CR, Zangari SI, Avila S, Williams D, Thaker TM, Tomasiak TM. The structural basis for regulation of the glutathione transporter Ycf1 by regulatory domain phosphorylation. *Nat Commun.* **13**, 1278 (2022).
60. Wang G The network basis for the structural thermostability and the functional thermoactivity of aldolase B. *Molecules.* **28,** 1850 (2023).
61. Wang G. Network basis for the heat-adapted structural thermostability of bacterial class II fructose bisphosphate aldolase. *ACS Omega.* **8,** 17731–17739 (2023).
62. Wang G. Thermal ring-based heat switches in hyperthermophilic class II bacterial fructose aldolase. *ACS Omega.* **8**, 24624–24634 (2023).
63. Wang G. Phosphatidylinositol-4,5-biphosphate (PIP_2)-Dependent Thermoring Basis for Cold-Sensing of the Transient Receptor Potential Melastatin-8 (TRPM8) Biothermometer. *Physchem.* **4,** 106–119 (2024).
64. Wang G. Thermoring basis for heat unfolding-induced inactivation in TRPV1. *Nat. Sci.***4**, e20240008 (2024).
65. Floyd R. W. Algorithm-97 - Shortest path. *Commun Acm.* **5,** 345–345 (1962).

AUTHOR CONTRIBUTIONS

Guangyu Wang wrote the main manuscript text and prepared Figures. 1, 2, 3, 4, 5, 6, 7 and Table 1 and Supporting Information (Tables S1, S2, S3), and reviewed the manuscript.

ACKNOWLEDGEMENTS

The author's own studies cited in this article were supported by the NIDDK Grant (DK45880 to D.C.D.) and the Cystic Fibrosis Foundation grant (DAWSON0210), the NIDDK grant (2R56DK056796-10) and the American Heart Association (AHA) Grant (10SDG4120011 to GW).

CONFLICT OF INTEREST STATEMENT

The author declares no conflict of interest.

ETHICS STATEMENT

The author confirms that he has followed the ethical policies of the journal.

DATA AVAILABILITY STATEMENT

All data generated or analyzed during this study are included in this published article and Supporting Information.

ORCID Guangyu Wang https://orcid.org/0000-0002-5581-6926

SUPPLEMENTARY INFORMATION

Additional supporting information can be found online in the Supporting Information section at the end of this article.

Table 1 Grid thermodynamic model-based new parameters of NBD1 in hCFTR constructs.

Construct	hCFTR		
PDB ID	5UAK	6MSM	6EIQ
F508	+	+	-
E1371Q	-	+	+
Mg/ATP (10 mM)/PKA	-	+	+
Sampling temperature, °C	4	4	4
NBD dimerized	-	+	+
Name of the biggest grid	$Grid_{21}$	$Grid_{8}$	$Grid_{12}$
Grid size (s)	21	8	12
# of energetically equivalent basic H-bonds (n) controlled by $Grid_s$	2.0	1.5	1.5
Total non-covalent interactions (N)	19	35	34
Total grid sizes (S), a.a.	104	76	83
Systematic thermal instability (T_i)	5.47	2.17	2.44
Calculated T_m, °C	**32**	**53**	**45**
Measured threshold T_m, °C*	**32**	**48**	**40**
References for measured T_m	(9)	(9, 28)	(9)

Note: measured thresholds are based on the isolated hNBD1-Δ(RE, RI).

FIGURES

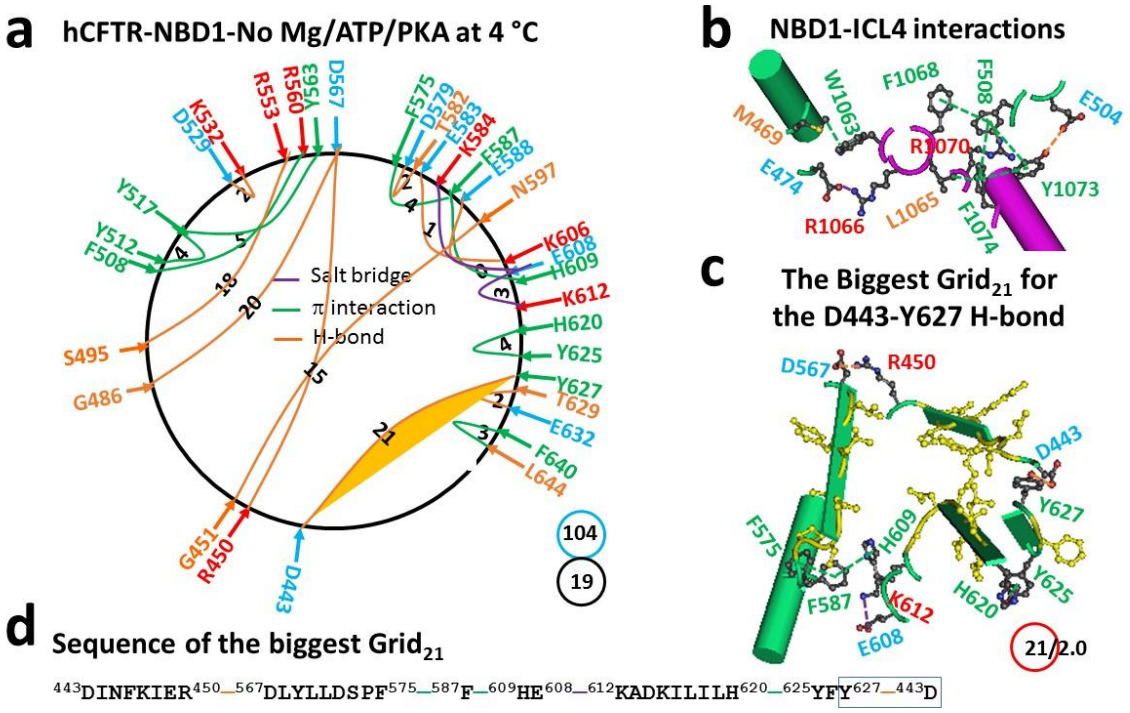

Figure 1. The thermoring structures of dephosphorylated hCFTR with F508 in the closed state at 4 °C. (**a**) The grid-like noncovalently interacting mesh network based on the cryo-EM structure of hCFTR with F508 in the absence of Mg/ATP/PKA at 4 °C (PDB ID, 5UAK, 3.87 Å). Salt bridges, H-bonds and π interactions are colored purple, orange, and green, respectively. The black numbers label the constrained grid sizes needed to control the least-stable noncovalent interactions in the grids. The least-stable D443-Y627 H-bond in the biggest $Grid_{21}$ is highlighted. The total grid sizes and the total grid size-controlled noncovalent interactions along the single peptide chain of NBD1 from E384 to M645 are shown in cyan and black circles, respectively. (**b**) Noncovalent interactions at the NBD1/ICL4 interface. (**c**) The structure of the biggest $Grid_{21}$ with a 21-residue size to control the least-stable D443-Y627 H-bond. The grid size and the equivalent basic H-bonds for the least-stable noncovalent interaction are shown in and near a red circle. (**d**) The sequence of the biggest $Grid_{21}$ to control the least-stable D443-Y627 H-bond in the blue box.

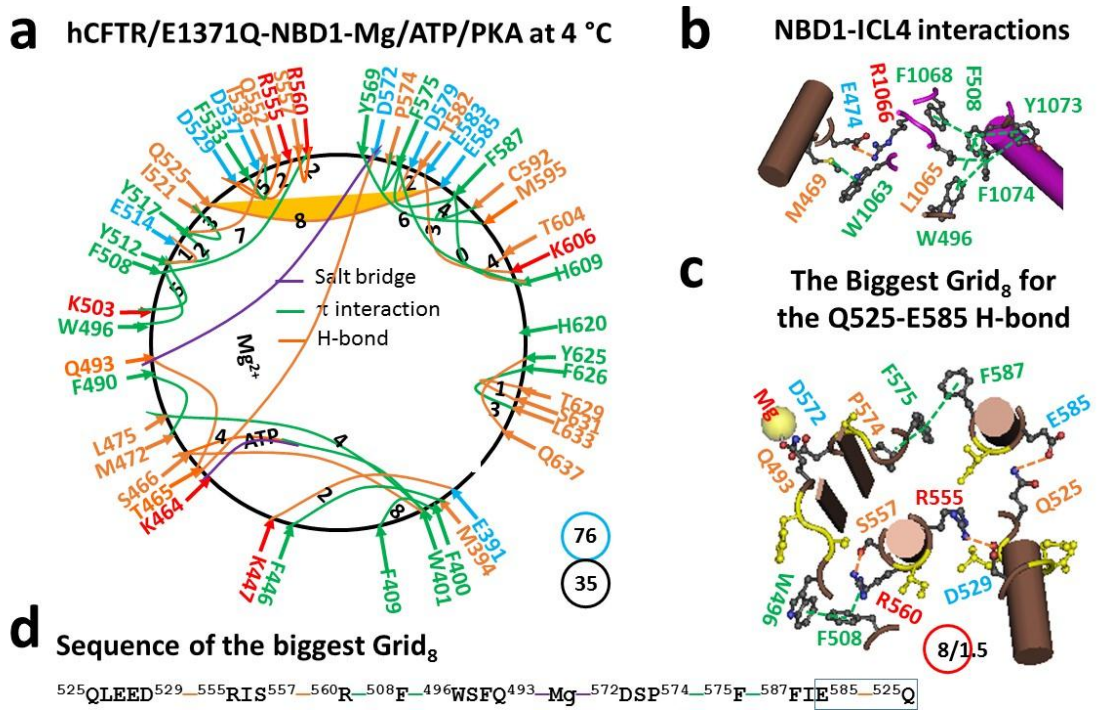

Figure 2. The thermoring structures of phosphorylated hCFTR/E1371Q with F508 in the open state at 4 °C. (**a**) The grid-like noncovalently interacting mesh network based on the cryo-EM structure of hCFTR/E1371Q with F508 in the presence of Mg/ATP/PKA at 4 °C (PDB ID, 6MSM, 3.2 Å). Salt bridges, H-bonds and π interactions are colored purple, orange, and green, respectively. The constrained grid sizes required to control the least-stable noncovalent interactions in the grids are labeled with black numbers. The least-stable Q525-E585 H-bond in the biggest $Grid_8$ is highlighted. The total grid sizes and the total grid size-controlled noncovalent interactions along the single peptide chain of NBD1 from E384 to Q637 are shown in cyan and black circles, respectively. (**b**) Noncovalent interactions at the NBD1/ICL4 interface. (**c**) The structure of the biggest $Grid_8$ with an 8-residue size to control the least-stable Q525-E585 H-bond. The grid size and the equivalent basic H-bonds for the least-stable noncovalent interaction are shown in and near a red circle. (**d**) The sequence of the biggest $Grid_8$ to control the least-stable Q525-E585 H-bond in the blue box.

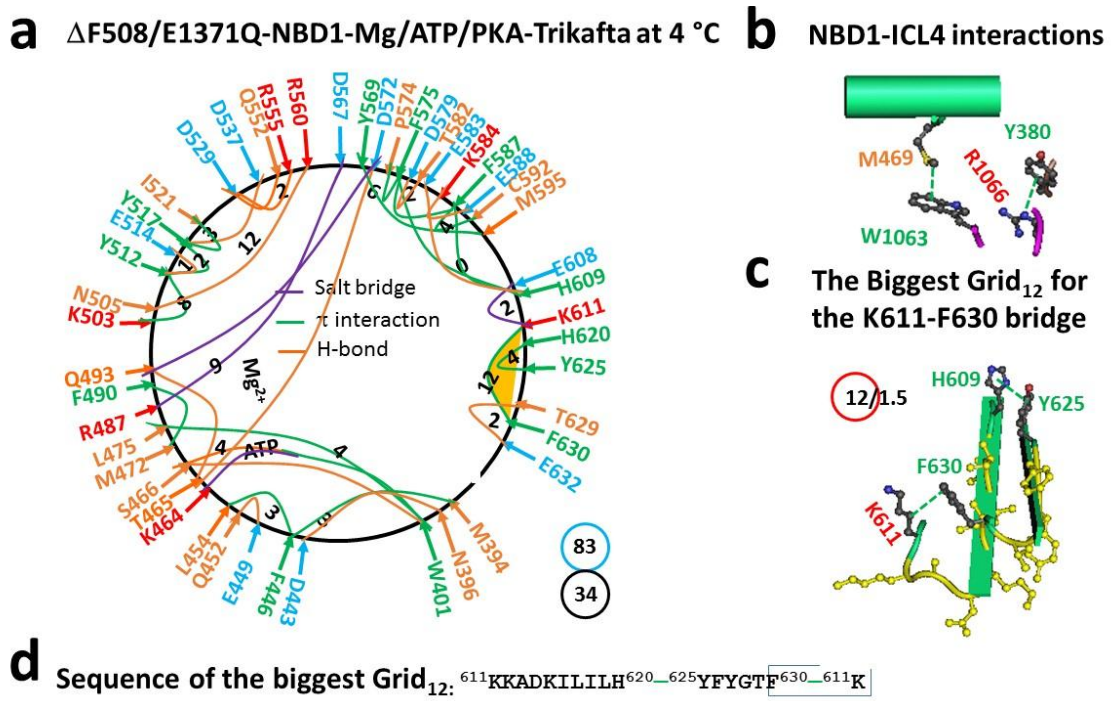

Figure 3. The thermoring structures of phosphorylated hCFTR/E1371Q/ΔF508 with Trikafta bound in the open state at 4 °C. (**a**) The grid-like noncovalently interacting mesh network based on the cryo-EM structure of hCFTR/E1371Q/ΔF508 with Trikafta bound in the presence of Mg/ATP/PKA at 4 °C (PDB ID, 8EIQ, 3.0 Å). Salt bridges, H-bonds and π interactions are colored purple, orange, and green, respectively. The constrained grid sizes required to control the least-stable noncovalent interactions in the grids are labeled with black numbers. The least-stable K611-F630 π interaction in the biggest $Grid_{12}$ is highlighted. The total grid sizes and the total grid size-controlled noncovalent interactions along the single peptide chain of NBD1 from L383 to L636 are shown in cyan and black circles, respectively. (**b**) Noncovalent interactions at the NBD1/ICL4 interface (Y380 is at the TMD1-NBD1 linker). (**c**) The structure of the biggest $Grid_{12}$ with a 12-residue size to control the least-stable K611-F630 π interaction. The grid size and the equivalent basic H-bonds for the least-stable noncovalent interaction are shown in and near a red circle. (**d**) The sequence of the biggest $Grid_{12}$ to control the least-stable K611-F630 π interaction in the blue box.

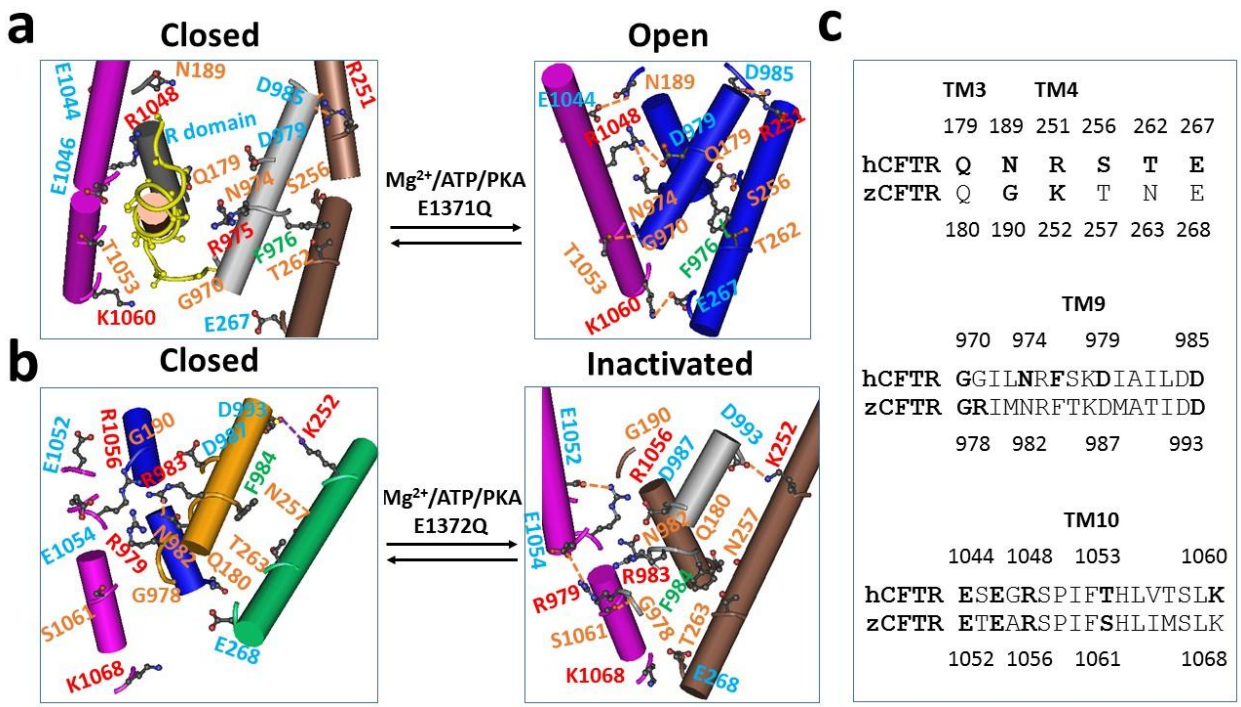

Figure 4. TMD1-TMD2 interactions at the gating center of CFTR (dashed lines). (a). Noncovalent interactions of hCFTR at the gating center in a closed dephosphorylated state (PDB, 5UAK) and a phosphorylated and Mg/ATP-bound open state (PDB, 6MSM). The R domain at the gating center is highlighted. (b). Noncovalent interactions of zCFTR at the gating center in a closed dephosphorylated state (PDB, 5TSI) and a phosphorylated and Mg/ATP-bound inactivated state (PDB, 5W81). (c). Sequence alignment of hCFTR and zCFTR.

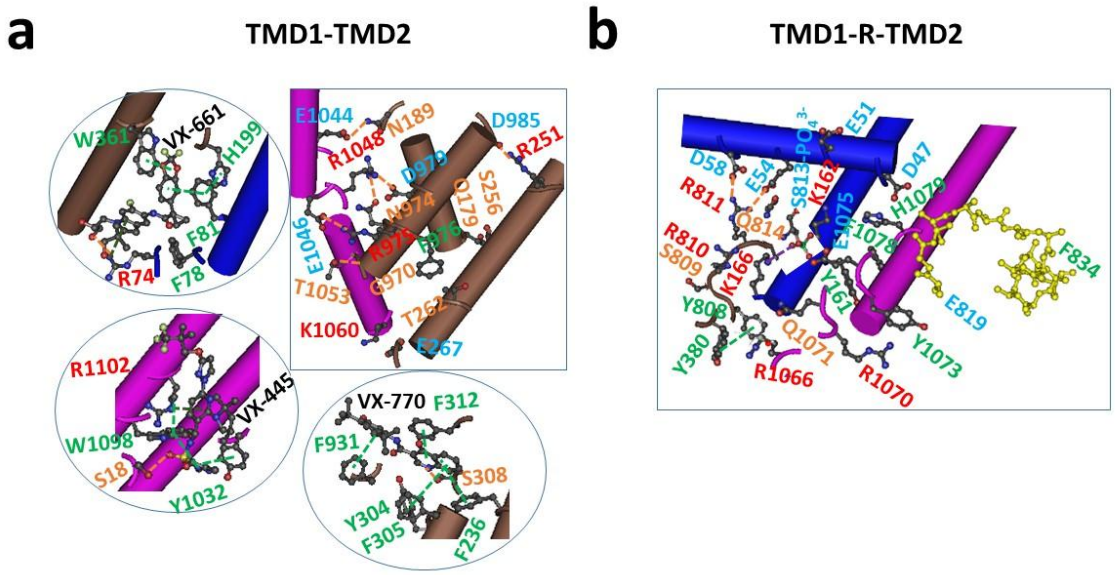

Figure 5. Effects of Trikafta on the phosphorylation-dependent noncovalent interactions (dashed lines) at the TMD1-TMD2 interface (a) and the TMD1-R-TMD2 interfaces (b) around the gating center of open ΔF508-hCFTR. The cryo-EM structures of phosphorylated E1371Q/ΔF508/hCFTR with Mg/ATP/Trikafta bound (PDB, 8EIQ) and Mg/ATP/PKA-C bound (PDB, 9DW9) in the open state are used for the models. The binding sites of three modulators (VX-445, VX-661 and VX-770) are shown around the gating center (a), and the segment E819-F834 of the R domain is highlighted in yellow (b).

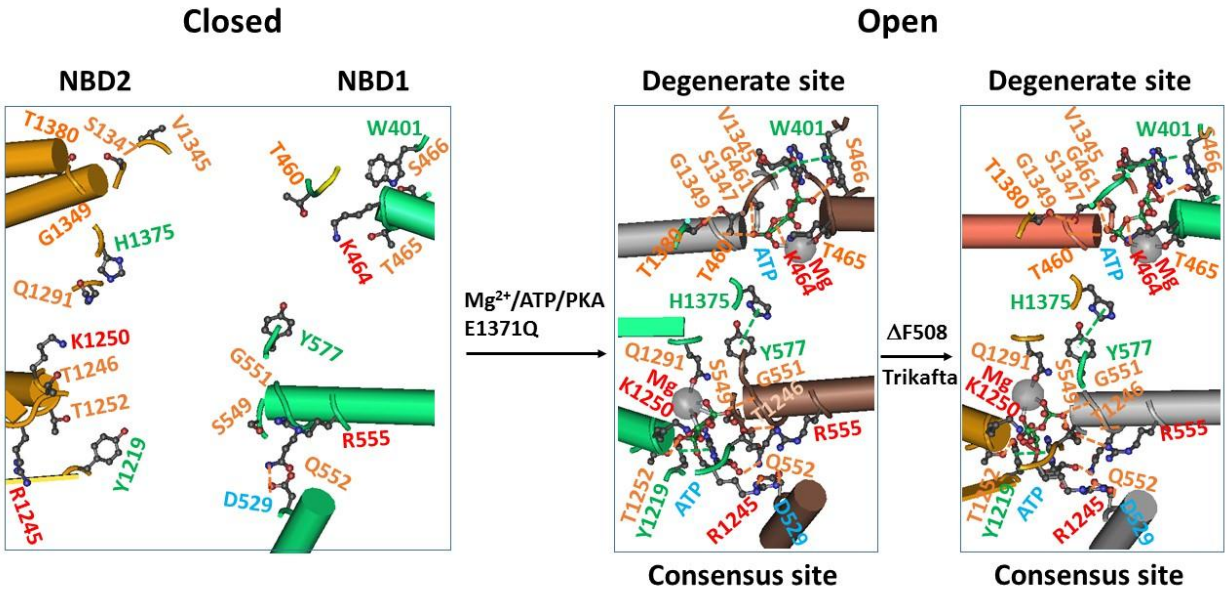

Figure 6. Effects of Trikafta on the ATP/PKA-dependent noncovalent interactions (dashed lines) between NBD1 and NBD2 near the gating center of open ΔF508-CFTR. Cryo-EM structures of dephosphorylated closed hCFTR (PDB, 5UAK), phosphorylated and Mg/ATP bound E1371Q/CFTR with (PDB, 6MSM) and without F508/Trikafta (PDB, 8EIQ) in the open state are used for the models.

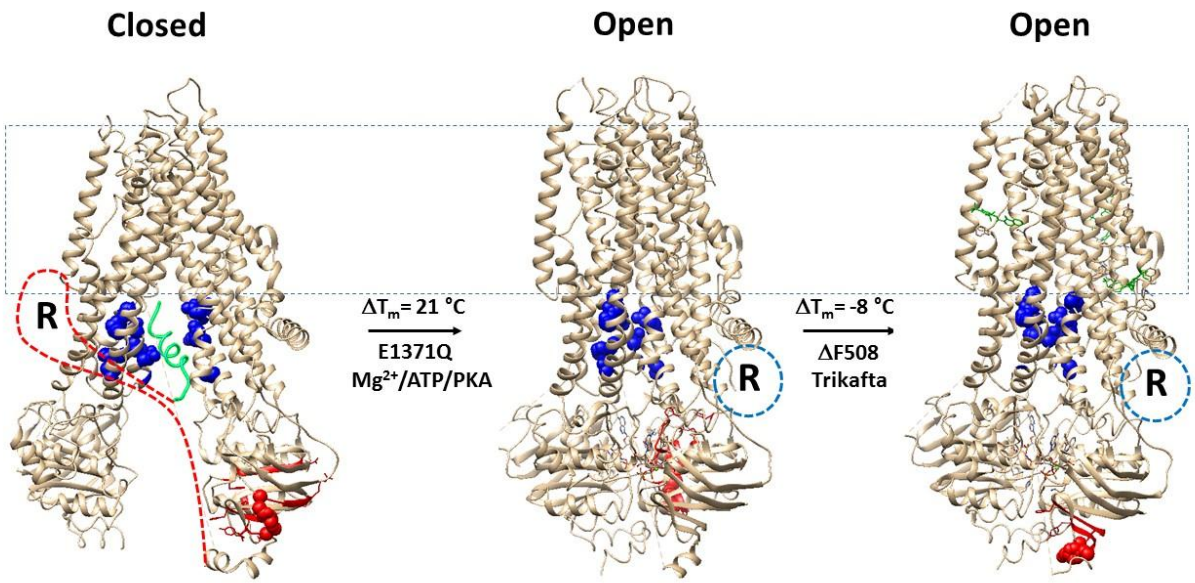

Figure 7. Putative Pathway for Trikafta to correct the primary gating and subsequent thermal defects of ΔF508-CFTR. Cryo-EM structures of dephosphorylated hCFTR (PDB: 5UAK), phosphorylated hCFTR/E1371Q with Mg/ATP bound in the absence (PDB: 6MSM) and presence of F508 and Trikafta (PDB: 8EIQ) are used for the models. The red curves and the blue circles represent the dephosphorylated and phosphorylated R domain, respectively. The N-terminal region of the R domain at the gating center (blue) is highlighted in cyan. Three modulators such as VX-445, VX-661 andVX-770 are colored green and the biggest thermorings in NBD1 are shown in red. The residues responsible for the least-stable noncovalent interactions in NBD1 are shown in space fills.